JOURNAL OF GEOPHYSICAL RESEARCH: SOLID EARTH, VOL. 118, 1–16, doi:10.1002/2013JB010215, 2013

On the effects of thermally weakened ductile shear zones on postseismic deformation

Christopher S. Takeuchi[1] and Yuri Fialko[1]

Received 20 March 2013; revised 25 October 2013; accepted 29 October 2013.

[1] We present three-dimensional (3-D) numerical models of postseismic deformation following repeated earthquakes on a vertical strike-slip fault. Our models use linear Maxwell, Burgers, and temperature-dependent power law rheology for the lower crust and upper mantle. We consider effects of viscous shear zones that result from thermomechanical coupling and investigate potential kinematic similarities between viscoelastic models incorporating shear zones and elastic models incorporating rate-strengthening friction on a deep aseismic fault root. We find that the thermally activated shear zones have little effect on postseismic relaxation. In particular, the presence of shear zones does not change the polarity of vertical displacements in cases of rheologies that are able to generate robust postseismic transients. Stronger rheologies can give rise to an opposite polarity of vertical displacements, but the amplitude of the predicted transient deformation is generally negligible. We conclude that additional (to thermomechanical coupling) mechanisms of strain localization are required for a viscoelastic model to produce a vertical deformation pattern similar to that due to afterslip on a deep extension of a fault. We also investigate the discriminating power of models incorporating Burgers and power law rheology. These rheologies were proposed to explain postseismic transients following large ($M7$) earthquakes in the Mojave desert, Eastern California. Numerical simulations indicate that it may be difficult to distinguish between these rheologies even with high-quality geodetic observations for observation periods less than a decade. Longer observations, however, may potentially allow discrimination between the competing models, as illustrated by the model comparisons with available GPS and interferometric synthetic aperture radar data.

Citation: Takeuchi, C. S., and Y. Fialko (2013), On the effects of thermally weakened ductile shear zones on postseismic deformation, *J. Geophys. Res. Solid Earth*, *118*, doi:10.1002/2013JB010215.

1. Introduction

[2] Large earthquakes are often followed by spatially and temporally varying deformation as the Earth's crust and mantle respond to stress perturbations produced by coseismic slip. Imaging of this transient deformation has dramatically improved in recent years as the density of GPS and interferometric synthetic aperture radar (InSAR) observations has increased in both time and space around seismogenic faults. The primary mechanisms invoked to explain postseismic deformation include viscoelastic relaxation [*Elsasser*, 1969; *Nur and Mavko*, 1974; *Savage and Prescott*, 1978], aseismic fault creep [*Ruina*, 1983; *Tse and Rice*, 1986], and poroelastic rebound [*Booker*, 1974; *Jonsson et al.*, 2003]. Poroelastic relaxation and shallow afterslip are upper crustal processes that have predominantly near-field effects, while deeper afterslip and viscoelastic relaxation occur mainly in the lower crust and upper mantle and thus produce broad-ranging surface displacements.

[3] The individual contributions of these mechanisms to postseismic relaxation following a given event may be difficult to identify, largely due to the nonuniqueness of inverse models. For instance, for an infinitely long strike-slip fault undergoing uniform coseismic displacement, viscoelastic relaxation predicts surface deformation that is indistinguishable from that due to an appropriately configured elastic dislocation model [*Savage*, 1990]. It was proposed that in the case of three-dimensional (3-D) deformation due to finite ruptures, the afterslip and viscoelastic relaxation mechanisms may in principle be distinguished as these mechanisms predict vertical postseismic velocity patterns that are opposite in polarity [e.g., *Pollitz et al.*, 2001]. In addition, viscoelastic relaxation models typically predict relatively large fault-normal velocities along strike from a finite strike-slip rupture, while such velocities are small or absent in afterslip models [*Hearn*, 2003]. However,

Additional supporting information may be found in the online version of this article.

[1]Institute of Geophysics and Planetary Physics, Scripps Institution of Oceanography, University of California, San Diego, La Jolla, California, USA.

Corresponding author: C. S. Takeuchi, Scripps Institution of Oceanography, UCSD, 9500 Gilman Dr. 0225, La Jolla, CA 92093-0225, USA. (ctakeuchi@ucsd.edu)

2169-9313/13/10.1002/2013JB010215

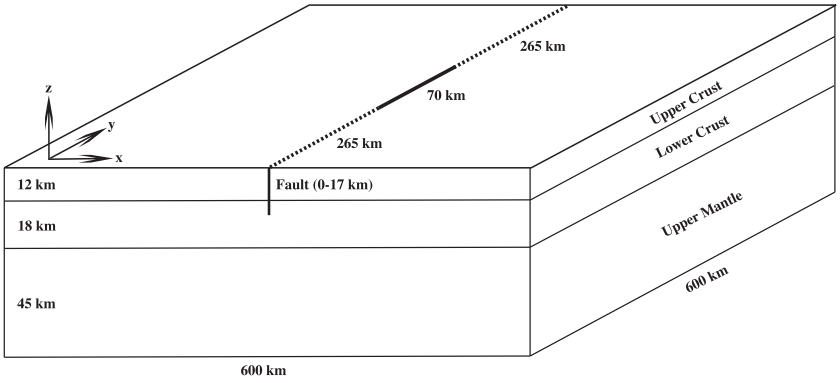

Figure 1. Model geometry.

if multiple mechanisms contribute to postseismic relaxation, even high-quality observations may not allow for robust discrimination between the candidate mechanisms. For example, postseismic deformation in the Eastern California Shear Zone (ECSZ) following the 1992 M_w7.3 Landers and 1999 M_w7.1 Hector Mine earthquakes has been ascribed to viscoelastic relaxation [*Pollitz*, 2003; *Freed and Bürgmann*, 2004], a combination of poroelastic relaxation and afterslip [*Peltzer et al.*, 1998; *Fialko*, 2004a], poroelastic and viscoelastic relaxation [*Masterlark and Wang*, 2002], as well as other mechanisms [*Massonnet et al.*, 1996; *Jacobs et al.*, 2002].

[4] Afterslip on the deep extension of the rupture plane may be considered to be kinematically analogous to a narrow ductile shear zone, with shear deformation governed by the constitutive equation for stress-driven frictional afterslip rather than that for viscoelastic flow [e.g., *Barbot et al.*, 2009]. Several previous investigations of postseismic relaxation have allowed for strain localization in the viscoelastic medium by incorporating a tabular region of reduced effective viscosity along the fault root [e.g., *Kenner and Segall*, 2003; *Freed et al.*, 2007; *Hearn et al.*, 2009]. However, the introduction of such shear zones into numerical models is usually ad hoc and neglects details of how such zones formed in the first place. In a previous study, we demonstrated that shear heating and thermomechanical coupling in the ductile substrate give rise to long-lived localized shear zones beneath mature strike-slip faults [*Takeuchi and Fialko*, 2012]. These shear zones participate both in loading faults interseismically and relaxing coseismic stress perturbations. Here we extend our 2-D results to 3-D finite-rupture scenarios. We use our models to test the hypothesis that under assumptions of laboratory-derived rheologies and far-field loading, a model incorporating highly localized ductile shear zone produced by shear heating may produce a postseismic deformation field similar to that predicted by a frictional afterslip model. In this case, different patterns of postseismic deformation might be expected depending on the effective fault age and slip rate, with afterslip-like localized viscoelastic shear dominating postseismic relaxation in the case of mature faults and diffuse viscoelastic relaxation dominating in the case of immature faults. We find that contrary to the hypothesis, thermally induced shear zones have little effect on postseismic relaxation. It follows that the degree of shear localization necessary for a viscoelastic relaxation model to mimic postseismic surface deformation due to frictional afterslip model requires additional strain-softening mechanisms.

2. Model Description

2.1. Geometry

[5] Most of the numerical simulations presented in this study were carried out using the finite element software Abaqus/Simulia (www.simulia.com/products/abaqus_fea.html). The model domain is a 600 km (fault normal, x coordinate) × 600 km (along strike, y coordinate) × 75 km (vertical, z coordinate) rectangular block (Figure 1). The domain is composed of three horizontal rheological layers: a 12 km thick elastic upper crust overlying an 18 km thick viscoelastic lower crust and a 45 km thick viscoelastic upper mantle. A 600 km long (y = –300 to 300 km) vertical planar fault is introduced within the domain at x = 0. The fault penetrates through the entire upper crust and roots in the lower crust at a depth of 17 km.

[6] The model domain is discretized into 612,000 elements, with 34 element layers in the fault-normal direction, 240 layers in the strike direction, and 75 vertical layers. Fault-normal node spacing decreases toward the fault, from 93.58 km in the far field to 0.5 km on the fault. Along-strike node spacing varies from 19.57 km in the far field to 0.5 km for $|y| > 35$ km; nodes are spaced by 0.5 km within $|y| \leq 35$ km. Nodes are spaced vertically by 1 km.

2.2. Rheology

[7] We explored four candidate rheologies of the viscoelastic lower crust and upper mantle. Two models incorporate linear rheologies for these layers. The first model incorporates a Maxwell rheology for the entire ductile substrate. The mantle has a viscosity η_m of 1.6×10^{17} Pa s, corresponding to the transient rheology of *Pollitz* [2003], and a shear modulus μ_m of 70 GPa. The lower crust in this model has a viscosity η_c of 3.2×10^{19} Pa s and a shear modulus μ_c of 38 GPa. Poisson's ratio is 0.25 in all model layers. We refer to this model as MS.

[8] The second model incorporating linear rheology assumes a biviscous Burgers body rheology, in which Maxwell and Kelvin viscoelastic elements are in series. This rheology requires that four parameters be defined: the steady state and transient viscosities η_1 and η_2, and the steady state and transient shear moduli μ_1 and μ_2. Details of the implementation of the Burgers rheology via the material's shear

Table 1. Laboratory-Derived Material Properties of Rocks

Rock Type	A (MPa^{-n} s^{-1})	n	Q (kJ mol^{-1})	ρ (kg m^{-3})	Ref.
Dry diabase	8.0	4.7	485	2850	a
Wet diabase	2.2×10^{-4}	3.4	260	2850	b
Dry olivine	1.1×10^{4}	3.5	535	3320	c
Wet olivine	3.6×10^{5}	3.5	480	3320	c

[a] *Mackwell et al.* [1998].
[b] *Shelton and Tullis* [1981].
[c] *Hirth and Kohlstedt* [2004].

relaxation modulus may be found in Appendix A. We select Burgers parameters $\eta_1 = 4.6 \times 10^{18}$ Pa s, $\eta_2 = 1.6 \times 10^{17}$ Pa s, $\mu_1 = 70$ GPa, and $\mu_2 = 70$ GPa, which were the best-fitting values of *Pollitz* [2003] for the rheology of the mantle beneath the Mojave Desert, California. We also use the best-fitting model of *Pollitz* [2003] for the lower crust, which incorporates a Maxwell rheology with a viscosity $\eta_c = 3.2 \times 10^{19}$ Pa s and a shear modulus $\mu_c = 38$ GPa (this value represents an average of the depth-varying shear modulus of *Pollitz* [2003] over our lower crustal depth range of 12–30 km). The lower crust for the biviscous-mantle model and the Maxwell-mantle model is thus identical. Poisson's ratio is 0.25 for all materials in the biviscous-mantle model. We refer to this model as BI.

[9] The remaining two models incorporate nonlinear, temperature-dependent rheology. In these models, the deviatoric strain rate $\dot{\varepsilon}_d$ and deviatoric stress σ_d in each finite element are related by the constitutive equation

$$\dot{\varepsilon}_d = A\sigma_d^n \exp\left(-\frac{Q}{RT}\right), \tag{1}$$

where R is the universal gas constant and the power law premultiplier A, the stress exponent n, and the activation energy Q are empirically determined constants [*Kirby and Kronenburg*, 1987]. The constitutive relation yields a stress- and temperature-dependent effective viscosity η_{eff} for each finite element

$$\eta_{\text{eff}} = \frac{\sigma_d}{2\dot{\varepsilon}_d} = \frac{1}{A\sigma_d^{n-1}} \exp\left(\frac{Q}{RT}\right). \tag{2}$$

We assume mafic (diabase) and ultramafic (olivine) compositions for the lower crust and upper mantle, respectively [*Rudnick and Fountain*, 1995; *Karato and Wu*, 1993]. To account for variability in ductile strength, we consider end-member models of hydrated (weak) and dry (strong) mineral compositions. Laboratory-determined material parameters for these models are listed in Table 1. In all power law models, the elastic behavior of both the upper crust and the ductile substrate is governed by the linear isotropic Hooke's Law, with a shear modulus and Poisson's ratio of 32 GPa and 0.25, respectively. The equivalent elastic and viscous elements of all viscoelastic constitutive relations other than Burgers are connected in series.

2.3. Thermal Regime

[10] To characterize the effects of thermally activated strain localization, we consider three different temperature regimes in our power law models. These temperature regimes modify the effective viscosity through the Arrhenius temperature dependence of the flow law (equations (1) and (2)). Strain will localize if the temperature below the fault is higher than that in the surrounding material.

[11] The first thermal model assumes a one-dimensional (1-D, i.e., only varying with depth) linear geotherm with a gradient of 20°C/km. The top and bottom surfaces have temperatures of 10°C and 1510°C, respectively. This geotherm is used for both models incorporating power law rheology; we refer to these models as WNS (wet/weak, no shear zone) and DNS (dry/strong, no shear zone). The second thermal model uses a 1-D piecewise-constant gradient corresponding to the maximum (in terms of the temperature at a given depth) geotherm of *Freed and Bürgmann* [2004], with top and bottom surface temperatures of 10°C and 1331°C, respectively. This temperature distribution corresponds to the best-fitting model of *Freed and Bürgmann* [2004] for the ductile substrate underlying the Mojave Desert, with a wet olivine mantle, a wet diabase lower crust, and a temperature of 1300°C at 50 km depth. The geotherm used in this model predicts higher temperatures and thus weaker ductile material at all depths above ~66 km relative to the linear 20°C/km geotherm. We refer to this model as WFB.

[12] The third thermal model includes localized shear zones around the downdip extension of the fault. The shear zones for each power law composition are generated using a model of long-term fault slip, during which heat conduction and viscous dissipation modify the initially 1-D 20°C/km geotherm. During each modeled time increment in the third thermal model, viscous dissipation generates internal energy within each finite element,

$$\rho H = \sigma_{ij}\dot{\varepsilon}_{ij}, \tag{3}$$

where ρ is density, H is the internal heat production per unit mass, and σ_{ij} and $\dot{\varepsilon}_{ij}$ are the stress and viscous strain rate (total strain rate less elastic strain rate) tensors, respectively (repeating indices imply summation). This dissipative energy term then contributes to changes in temperature within each element as governed by conservation of energy,

$$\sigma_{ij}\dot{\varepsilon}_{ij} + k\nabla^2 T = \rho c_p \frac{\partial T}{\partial t}, \tag{4}$$

where k is the thermal conductivity and c_p is the specific heat capacity of the material in the element. This energy balance produces a temperature increment $\Delta T = \Delta T_v + \Delta T_c$, with a contribution ΔT_v from viscous dissipation

$$\Delta T_v = \int_{t_i}^{t_f} \frac{1}{\rho c} \sigma_{ij}\dot{\varepsilon}_{ij} \mathrm{d}\tau \tag{5}$$

and a contribution ΔT_c from heat conduction

$$\Delta T_c = \int_{t_i}^{t_f} \kappa \nabla^2 T \mathrm{d}\tau, \tag{6}$$

where $\kappa = k/\rho c$ is the thermal diffusivity and t_i and t_f are the initial and final times of the time increment, respectively. The temperature increment adds to the total temperature in the finite element and updates the effective viscosity of the material in the element through equation (2). The thermal evolution has a duration of 20 Myr and thus simulates the thermal conditions expected for a mature fault. Further details of the setup simulating the long-term thermal evolution may be found in *Takeuchi and Fialko* [2012]. Figure 2 shows the structure of the shear zones developed in

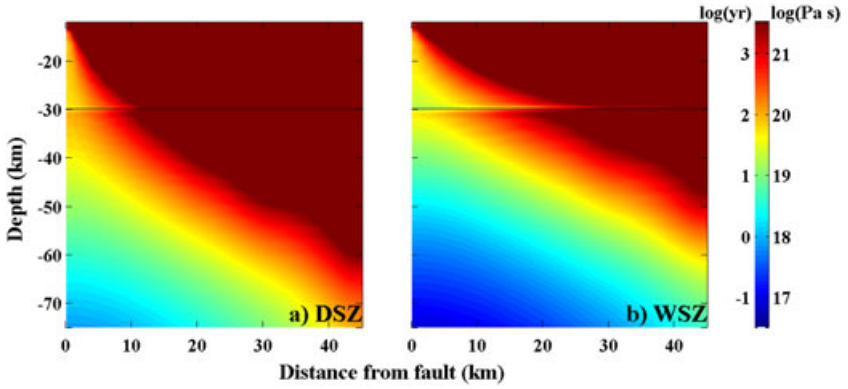

Figure 2. Effective viscosity and relaxation times for models (a) DSZ and (b) WSZ. Relaxation times are calculated using $t_r = \frac{\eta_{\text{eff}}}{G}$ where $\eta_{\text{eff}} = \frac{\sigma_d}{2\dot{\varepsilon}_d}$ is the effective viscosity and $G = 32$ GPa is the shear modulus.

Takeuchi and Fialko [2012] in terms of the effective viscosity (equation (2)) and relaxation time $t_r = \frac{\eta_{\text{eff}}}{G}$, where G is the assumed shear modulus of the substrate (32 GPa).

[13] Calculations of *Takeuchi and Fialko* [2012] made use of symmetries of the 2-D problem. For the current study, the thermal structures generated by *Takeuchi and Fialko* [2012] for each power law model are extruded along strike, so that the x–z cross sections of the temperature field at each along-strike (y) coordinate are identical. As viscous dissipation and heat conduction are symmetric with respect to the fault plane, the one-sided temperature fields are mirrored across the fault to provide temperature conditions for each node in the mesh for each power law model. These symmetric temperature distributions are then used as thermal boundary conditions for the respective power law models. We refer to these models as WSZ (wet/weak, with shear zone) and DSZ (dry/strong, with shear zone). Table 2 summarizes the rheological and thermal parameters assumed in this study.

2.4. Earthquake Simulations

[14] In this study we employ kinematically driven earthquake cycles, i.e., coseismic fault slip is prescribed as a boundary condition. Such models generate unphysical stresses in the lithosphere; in particular, repeated kinematically prescribed earthquakes produce negative (i.e., having sense opposite to that of fault slip) stresses in the seismogenic layer [*Takeuchi and Fialko*, 2012]. However, surface velocities resulting from viscoelastic relaxation are relatively insensitive to the type of boundary condition on a fault surface [*Takeuchi and Fialko*, 2012]. We include gravity in our 3-D models as it can influence surface deformation, primarily by suppressing long-wavelength vertical displacements late in the interseismic period [*Pollitz*, 1997]. Gravity is implemented as a body force in the stress equilibrium equations,

$$\sigma_{ij,j} + \rho g_i = 0, \tag{7}$$

where ρ is density, $g_i = (0, 0, -g)$ is the gravitational acceleration (assuming a positive upward z coordinate, Figure 1) and the comma in the first term represents differentiation. We also apply an initial lithostatic stress field

$$\sigma_l = \int_0^h \rho(z) g dz, \tag{8}$$

where h is the depth at the center of a given finite element; the initially piecewise-linear lithostatic stresses are equilibrated in an initial model step. We simulate tectonic loading by imposing constant slip rate of 40 mm/yr within the upper 12 km (corresponding to the thickness of the elastic layer) of the 600 km fault for 100 kyr. Velocities of 20 mm/yr are prescribed at the far-field boundaries of the model domain ($x = \pm 300$ km). Fault slip is cosine tapered from the full slip rate at 12 km to zero at 17 km depth in order to prevent a stress singularity due to the abrupt termination of fault slip at the base of the elastic layer.

[15] This initial model is followed by 10 earthquake cycles on the entire 600 km long fault. In these cycles, we

Table 2. Model Configurations[a]

Model Configuration	Lower Crustal Rheology	Upper Mantle Rheology	Thermal Regime
MS (Maxwell)	$\eta = 3.2 \times 10^{19}$ Pa s	$\eta = 1.6 \times 10^{17}$ Pa s	N/A
BI (Burgers)	$\eta = 3.2 \times 10^{19}$ Pa s	$\eta_1 = 4.6 \times 10^{18}$ Pa s $\eta_2 = 1.6 \times 10^{17}$ Pa s	N/A
WFB (Power law)	Wet Diabase	Wet Olivine	Piecewise Linear[b]
WNS (Power law)	Wet Diabase	Wet Olivine	20 °C/km
WSZ(Power law)	Wet Diabase	Wet Olivine	Shear Zone[c]
DNS (Power law)	Dry Diabase	Dry Olivine	20 °C/km
DSZ (Power law)	Dry Diabase	Dry Olivine	Shear Zone[c]

[a]Seven viscoelastic model configurations are utilized in this study. Rheological parameters for diabase and olivine are summarized in Table 1.
[b]One-dimensional geotherm of *Freed and Bürgmann* [2004].
[c]Shear zone temperature structure of *Takeuchi and Fialko* [2012].

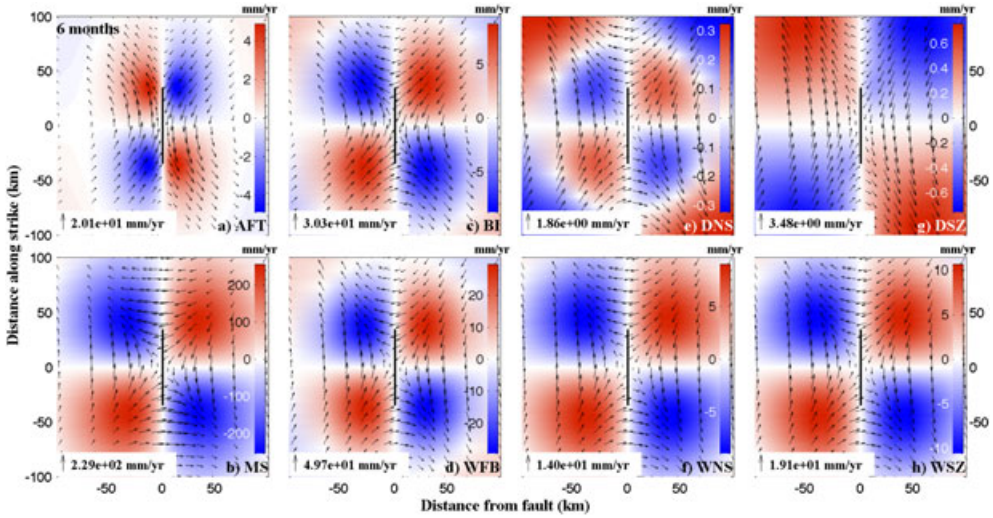

Figure 3. Map view of postseismic surface velocities in mm/yr, 6 months after rupture for models (a) AFT (afterslip), (b) MS (Maxwell), (c) BI (biviscous), (d) WFB (wet power law, *Freed and Bürgmann* [2004] thermal regime), (e) DNS (dry power law, no shear zone), (f) WNS (wet power law, no shear zone), (g) DSZ (dry power law, shear zone), and (h) WSZ (wet power law, shear zone). Colors indicate vertical velocity, and arrows indicate horizontal velocity (scales are indicated in each panel). Heavy black line denotes the fault plane.

prescribe an instantaneous coseismic slip of 8 m on the upper 12 km of the fault. Fault slip is again cosine tapered to zero at 17 km depth. We then lock the fault for an interseismic period of 200 years. The total relative plate velocity (40 mm/yr) is maintained on the far-field boundaries of the model domain at all times. Because deformation is antiplane strain, only fault-parallel motion is allowed. The total duration of the model spin-up (100 kyr tectonic loading followed by ten 200 year earthquake cycles) represents a compromise between full cycle invariance [e.g., *Hetland and Hager*, 2006; *Takeuchi and Fialko*, 2012] and computation time.

[16] Following the final interseismic period of the last system-wide earthquake, we simulate a finite rupture on a 70 km long segment in the middle of the domain ($|y| \leq$ 35 km). Slip amplitude is the same as in previous system-wide events. The respective moment is 1.08×10^{20} N m, similar to the moment estimates for the 1992 M_w7.3 Landers rupture [*Kanamori et al.*, 1992; *Sieh et al.*, 1993; *Fialko*, 2004b] and slightly higher than those for the 1999 M_w7.1 Hector Mine rupture [*Dreger and Kaverina*, 2000; *Simons et al.*, 2002]. During the coseismic step, the fault is not allowed to move in the fault perpendicular or vertical directions. Following the finite rupture, the entire fault is then locked for a duration of 200 years during which coseismic stress changes are allowed to relax. No vertical motion is allowed on the far-field model boundaries; normal displacements are also not allowed on the fault-parallel sides of the domain, while relative far-field velocities are maintained on these boundaries ($x = \pm 300$ km). Antiplane-strain conditions are also maintained on the model boundaries orthogonal to the slip direction ($y = \pm 300$ km). Deformation in all three dimensions is otherwise freely permitted inside the domain.

2.5. Afterslip Model

[17] For comparison, we also perform simulations of stress-driven afterslip of the deep extension of the fault using the fictitious body force code RELAX [*Barbot and Fialko*, 2010]. In this model, a fault of dimensions identical to those in the viscoelastic models is embedded within a 512 km × 512 km × 512 km elastic domain. An afterslip plane lies beneath and oriented with the fault; the plane is centered at $x = y = 0$ and is 150 km in length and 50 km downdip ($|y| \leq 75$ km, $17 \leq z \leq 67$ km). The slip velocity V on the afterslip plane is governed by rate-strengthening friction,

$$V = 2\dot{\gamma}_0 \sinh \frac{\Delta\tau}{(a-b)\sigma}, \tag{9}$$

where $(a-b)\sigma$ and $\dot{\gamma}_0$ are constitutive parameters, the former controlling the velocity dependence of friction and the latter the timescale of postseismic slip, and $\Delta\tau$ is the coseismic stress change. The a and b correspond to the parameters of rate- and state-dependent friction [e.g., *Ruina*, 1983; *Dieterich*, 1978]. Because in situ values of the model parameters are not well-constrained, the timescale of relaxation is rather arbitrary. The afterslip model will thus only be used for qualitative comparison. We adopt $(a-b)\sigma$=0.9 MPa and $\dot{\gamma}_0$=1 km/yr. The coefficient of friction μ_0 at the reference slip rate $\dot{\gamma}_0$ is 0.6. We refer to this model as AFT.

3. Results

3.1. Surface Velocity Patterns

[18] In this section we focus on theoretical predictions of surface deformation and the sensitivity of surface deformation to the assumed rheologies. We generate maps of postseismic velocity, from which contributions of secular deformation have been removed. We study the first 50 years of deformation, as postseismic velocities after this time are likely to fall below the detection limit, and there are few examples of geodetically documented long-lasting (>50 years) postseismic deformation transients. Figures 3–6 illustrate modeled postseismic surface velocities within 100 km of the fault for several epochs following coseismic

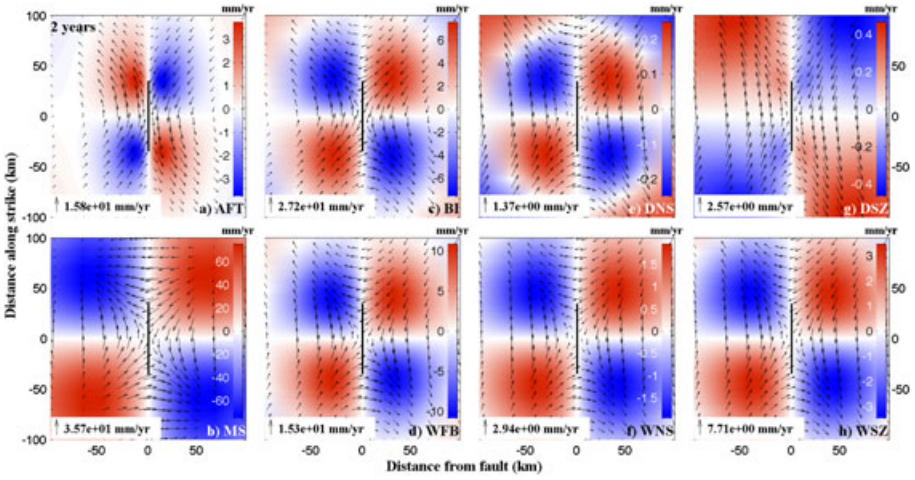

Figure 4. Postseismic surface velocities in mm/yr, 2 years after rupture. Panels as indicated in Figure 3 caption. Colors indicate vertical velocity, and arrows indicate horizontal velocity. Heavy black line denotes the fault plane.

rupture. Six months after the earthquake (Figure 3), each model shows a clear four-quadrant pattern of uplift and subsidence, though the polarity and amplitude of deformation vary. Model MS predicts the largest amplitudes of vertical velocity at this time epoch, as expected due to the short relaxation timescale of the substrate. Wet power law models all have similar vertical velocity patterns, though WFB has larger amplitudes and smaller wavelength lobes compared to models WNS and WSZ. Model DNS shows a similar pattern to the wet power law models, though amplitudes are an order of magnitude smaller, and relatively large vertical velocities are seen in the far field. Model DSZ shows similar amplitudes and far-field polarity as DNS, but the near-field polarity is reversed relative to all other viscoelastic models. Model AFT is the only other model showing near-field subsidence northeast and southwest of the finite rupture and uplift northwest and southeast of the rupture.

[19] Horizontal velocities 6 months following the earthquake show broadly similar qualitative patterns for all models, with quadrant patterns of combined right-lateral fault-parallel velocities and left-lateral fault-perpendicular velocities. As with vertical velocities, model MS predicts the largest amplitudes of horizontal velocity. Wet power law models are nearly indistinguishable except for the relatively large amplitudes for model WFB. Dry power law models predict horizontal velocities with an order of magnitude smaller than wet power law models. While horizontal velocity patterns are generally similar in all models, minor deviations from the common mode do exist for certain models. For instance, model AFT predicts horizontal velocities that have smaller relative amplitudes in the far field compared to viscoelastic models, as well as vanishing fault-perpendicular velocities near the along-strike extensions of the fault. Model MS predicts negligible fault-parallel velocities along strike from the fault. Model DSZ predicts large far-field velocities relative to the near field, as well as a relatively small fault-perpendicular component of velocity near the fault plane.

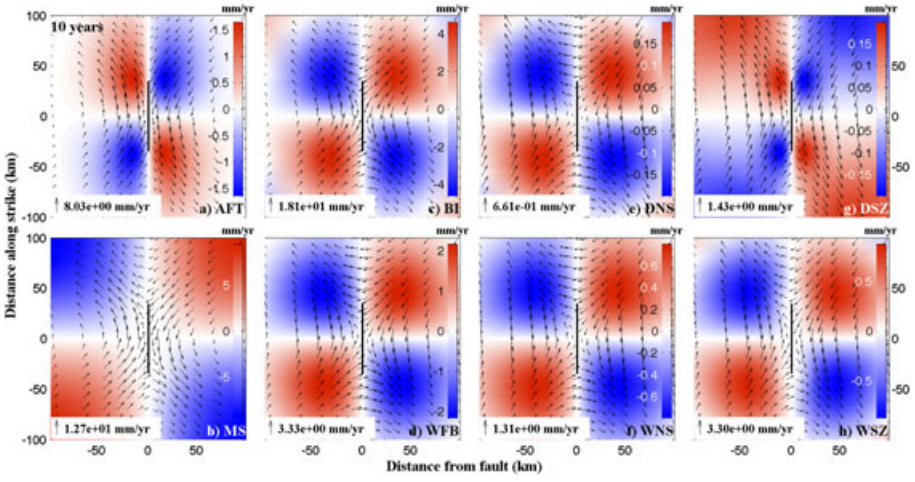

Figure 5. Postseismic surface velocities in mm/yr, 10 years after rupture. Panels as indicated in Figure 3 caption. Colors indicate vertical velocity, and arrows indicate horizontal velocity. Heavy black line denotes the fault plane.

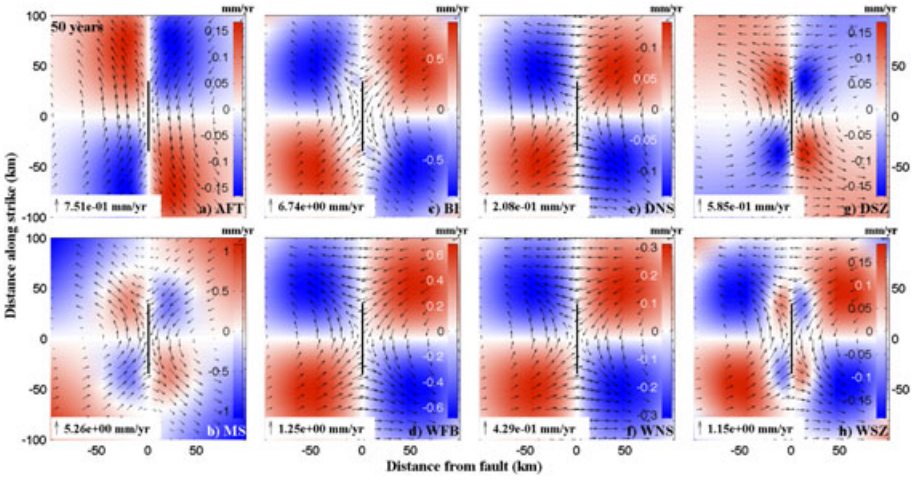

Figure 6. Postseismic surface velocities in mm/yr, 50 years after rupture. Panels as indicated in Figure 3 caption. Colors indicate vertical velocity, and arrows indicate horizontal velocity. Heavy black line denotes the fault plane.

[20] All models show a reduction in the amplitude of both vertical and horizontal surface velocities from 6 months to 2 years (Figure 4) as the transient deformation begins to decay. The percentage reduction is largest for model MS, which incorporates the weakest substrates. Velocity patterns and vertical polarity are maintained for all models other than MS; near-field vertical polarities remain reversed for models AFT and DSZ relative to all other models. Model MS shows that maximum vertical velocities within the four quadrants move away from the fault, illustrating a "strain wave" due to stress diffusion.

[21] Amplitudes of both horizontal and vertical velocities are further decreased for all models 10 years after the rupture (Figure 5). Velocity patterns and polarity are largely unchanged for model BI and all wet power law models. Models AFT and DNS illustrate expanded near-fault vertical velocity lobes. Models MS and DSZ show the most notable changes in vertical and horizontal velocities. In particular, model MS predicts continued outward movement of the initial vertical velocity quadrants and the initiation of a near-fault polarity reversal. Model DSZ predicts enhanced near-field vertical velocities compared to far-field velocities; near-field fault-parallel velocities are also enhanced relative to the far field.

[22] Fifty years after the rupture, all models except DNS, WFB, and WNS demonstrate significant evolution of the respective surface velocity patterns (Figure 6). Vertical velocity lobes in model AFT have expanded significantly toward the far field, reflecting propagation of afterslip toward deeper parts of the fault. Model BI predicts a low-amplitude reversed-polarity near-field vertical velocity pattern. Model DSZ shows significantly enhanced near-field vertical velocities relative to far-field velocities, as well as reduced far-field fault-parallel velocity and negligible fault-parallel velocity along strike from the rupture. Model MS predicts expansion of the 10 year reversed-polarity quadrant pattern toward the far field. Model WSZ shows the initiation of a reversed near-field vertical pattern. Vertical velocities at this epoch are very small (<1 mm/yr), likely below the geodetic detection limits. However, models BI and MS maintain appreciable horizontal velocities, reflecting ongoing response of the ductile substrate to coseismic stress changes even 50 years after the event.

4. Comparison With Data

4.1. Postseismic Deformation in the Mojave Desert

[23] One of the vivid examples of nonunique interpretations of geodetic data is deformation following the 1992 M_w7.3 Landers and 1999 M_w7.1 Hector Mine earthquakes in the Mojave Desert (eastern California). *Pollitz et al.* [2000, 2001] argued that the pattern of postseismic vertical velocities around the fault is consistent with relaxation in the upper mantle and opposite to that expected of afterslip. *Pollitz et al.* [2000, 2001] used models assuming linear Maxwell rheology, while *Freed and Bürgmann* [2004] argued that the nonexponential character of time series of postseismic displacements can be indicative of power law rheology. *Pollitz* [2003] proposed that a biviscous rheology can also explain observations. The best-fitting rheologies in these studies were chosen based on model fits to a few years of GPS data collected in the Eastern California Shear Zone (ECSZ). Alternatively, it was proposed that interferometric synthetic aperture radar (InSAR) and GPS observations of the two events can be interpreted in terms of a combination of afterslip and poroelastic rebound, such that afterslip dominates horizontal deformation and poroelastic rebound dominates vertical deformation [*Peltzer et al.*, 1998; *Fialko*, 2004a]. *Freed et al.* [2007] considered the effect of a ductile shear zone on far-field relaxation after the Hector Mine earthquake. Here we investigate whether longer observations can provide discrimination between the previously proposed deformation mechanisms. For this purpose, we consider extended records of GPS and InSAR data characterizing transient deformation following the Hector Mine earthquake. We note that the rheologies mentioned above were deduced from fitting the respective sets of geodetic data (e.g., in the case of *Pollitz* [2003] and *Freed and Bürgmann* [2004], the first < 3.2 years of Hector Mine postseismic GPS displacement data). Here we test the proposed rheological models against the extended GPS and InSAR data sets

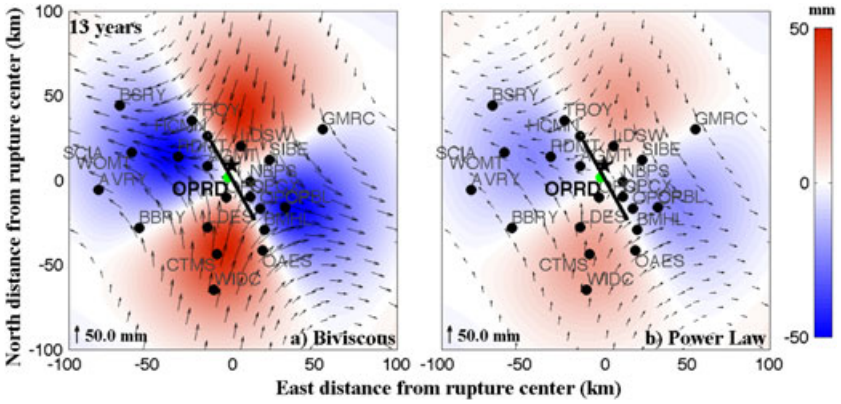

Figure 7. Thirteen years of surface displacement in millimeters following the simulated Hector Mine rupture. Colors indicate vertical displacement, and arrows indicate horizontal displacement. SCIGN continuous GPS stations with time series in Figures 8 and 9 shown by black circles, with station identifiers as indicated. Reference station (for horizontal displacements) OPRD denoted by green circle. Heavy black line denotes the simulated Hector Mine rupture. Black star denotes the epicenter of the Hector Mine earthquake.

that span more than 10 years of postseismic deformation. In doing so, we do not attempt to tune the model parameters to improve the data fit.

[24] We use a simplified model of the Hector Mine rupture that consists of a 54 km long vertical planar fault. We apply a uniform slip in the depth interval 0–9 km and cosine taper the slip to zero at 13 km depth. The average slip amplitude is chosen to match the seismic moment of the Hector Mine earthquake, 4–6 $\times$ 10^{19} N m [*Dreger and Kaverina*, 2000; *Simons et al.*, 2002]. These simplifications are justified as (i) coseismic stress changes at depth are sensitive to the earthquake moment and not to the details of slip distribution, and (ii) we are interested in the overall qualitative features of viscoelastic deformation. Our models incorporate the viscoelastic rheologies (and 1-D thermal regime in the case of power law rheology) used in models BI and WFB (for the purposes of distinguishing it from the previous WFB model, the latter Hector Mine model will be denoted "power law"), as well as the layered elastic structure used by *Pollitz* [2003]. Section 3 indicates that the presence of thermally activated shear zones has little effect on postseismic transients even in the case of relatively fast-slipping faults; for immature faults with low slip rates, such as those comprising the Eastern California Shear Zone [e.g., *Dokka and Travis*, 1990], strain localization due to thermomechanical coupling and its effects on surface deformation are expected to be smaller still. Therefore, we use a 1-D thermal structure and do not consider thermal shear zones in these calculations.

[25] We generate a tectonic background stress by applying a constant shear strain rate of 10^{-7} year^{-1} [*Savage et al.*, 2003] until the shear stress in the ductile substrate evolves to a steady state. In the case of the power law model, the thickness of the "elastic" upper crust is found to depend on the duration of tectonic loading. For longer loading periods, colder rocks with larger relaxation times begin to flow, and the effective thickness of the elastic-brittle lid decreases. We apply the tectonic loading in the power law model until the lid is 18 km thick (equal to the prescribed thickness of the elastic crust in the biviscous model of *Pollitz* [2003]) and the stress in the ductile substrate is constant. Numerical experiments showed that the model predictions are essentially insensitive to a longer duration of tectonic loading. The tectonic loading is applied parallel to the fault plane and thus differs by 10° in azimuth from the estimated regional direction of shear of N40°W [*Savage et al.*, 2003]. This difference is small and likely within the data uncertainty and has little effect on the qualitative features of the model. Following the tectonic loading, we simulate coseismic rupture and 50 years of postseismic relaxation. The modeled fault is aligned with the surface rupture of the Hector Mine earthquake, with an average strike of N30°W (Figure 7). We extract 13 year time series of displacement at locations of the continuous GPS stations and reference them to station OPRD (see Figure 7).

[26] We compare our model displacement time series to post-Hector Mine GPS time series from the Scripps Orbit Permanent Array Center (http://sopac.ucsd.edu) (Figures 8 and 9). The GPS time series are corrected for station location bias (the removal of which sets the beginning of the time series to zero), coseismic offsets, and annual and semiannual signals. Data referencing to a given site remove the contribution from the regional motion of the ECSZ with respect to a given reference frame. The relative GPS displacements therefore represent contributions due to postseismic and secular deformation only.

[27] We select station OPRD for site referencing based on the following arguments. First, site location near the rupture center allows for a better visualization of the predicted postseismic displacements. Second, we calculated the average model misfits for the east, north, vertical, as well as total displacement components, using each station as the reference site,

$$\chi_k^{\text{model}} = \frac{1}{N}\sum_{i=1}^{N}\left\{\frac{1}{L}\sum_{j=1}^{L}[(O_{i,j}-O_{k,j})-(M_{i,j}-M_{k,j})]^2\right\}^{\frac{1}{2}}, \quad (10)$$

where O and M are the observed and modeled displacements, respectively, index j represents displacement components, index i represents a site number, $N+1$ is the total number of sites, and index k corresponds to the reference site. The average of the values of χ_k^{BI} and χ_k^{WFB} for each reference station k

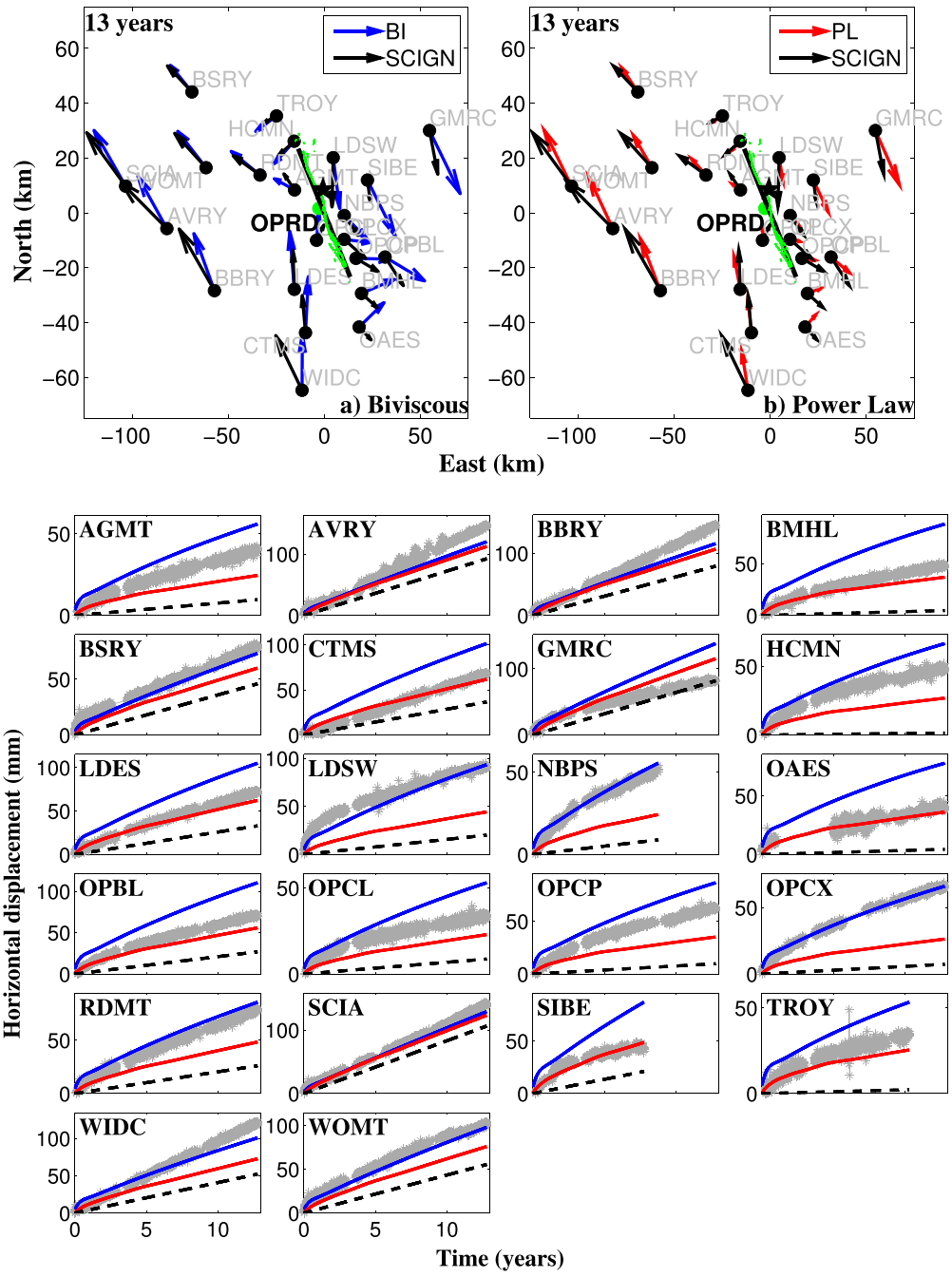

Figure 8. (a, b) Thirteen years of horizontal displacement in millimeters following the Hector Mine rupture. Displacements referred to continuous GPS station OPRD (green dot) and shown by black (observed), blue (biviscous model, Figure 8a), and red (power law model, Figure 8b) arrows. Black circles denote GPS station locations. Black star denotes the epicenter of the Hector Mine earthquake, heavy black line denotes the simulated Hector Mine rupture, and green line denotes the true Hector Mine rupture. Other panels show time series of observed (grey stars) and modeled (solid blue line = biviscous model, solid red line = power law model) horizontal displacement, referred to station OPRD, for stations as indicated in Figures 8a and 8b. Dashed black line denotes displacement due to modeled station secular velocity referred to simulated station OPRD.

are shown in the supporting information Figure S1a. As one can see from Figure S1a, station OPRD has a low-average total displacement misfit relative to nearly all other stations within the array considered and therefore is an "optimal" reference site for the chosen suite of models.

[28] Figures 8 and 9 show the observed OPRD-referenced horizontal and vertical GPS displacements along with predictions of models BI and WFB (Table 2). The biviscous model predicts quasi-constant horizontal velocities after robust transient deformation within the first ∼3 months.

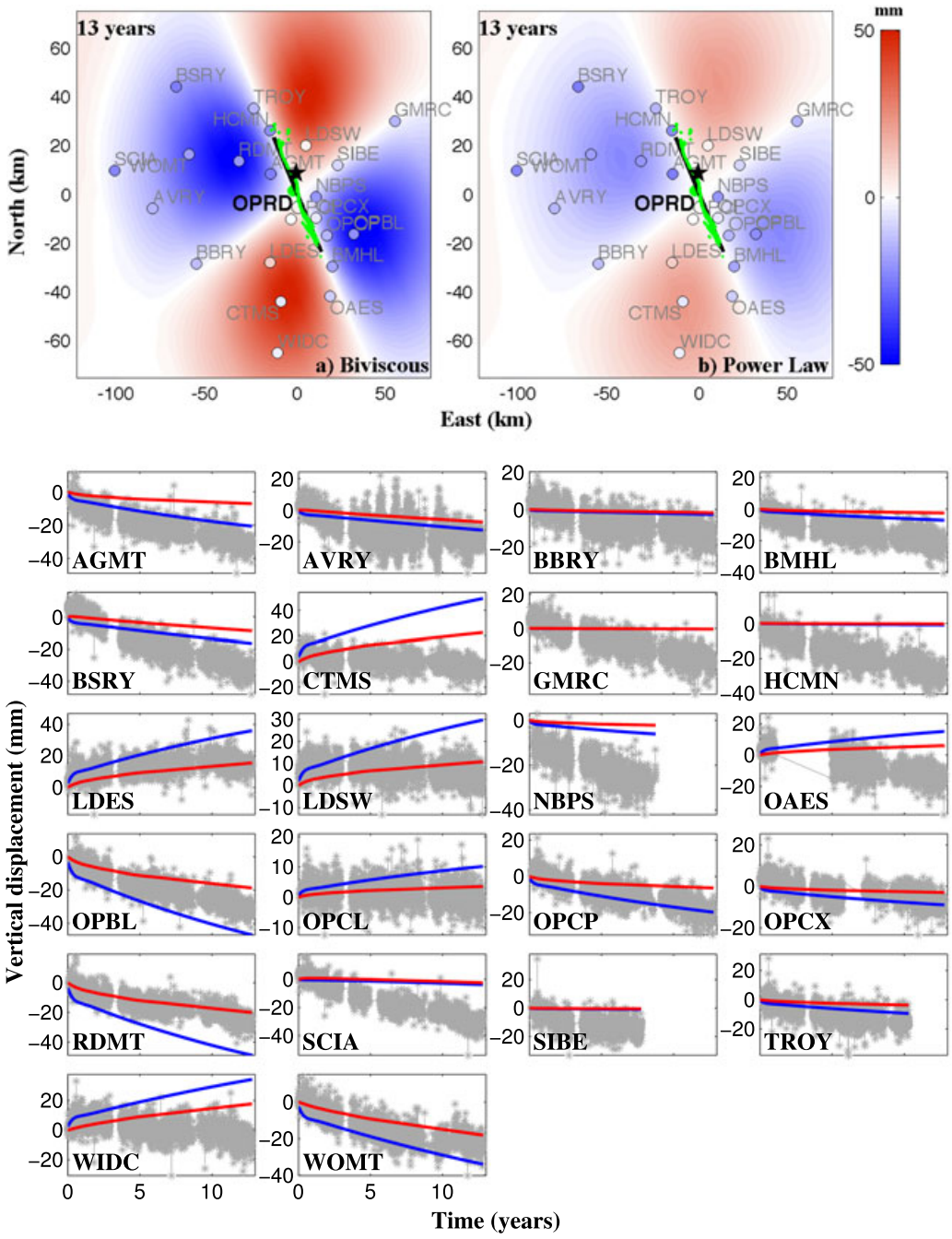

Figure 9. (a, b) Thirteen years of vertical displacement in millimeters following the Hector Mine rupture. Modeled and observed displacements shown by colors and colored circles at GPS station locations, respectively. Black star denotes the epicenter of the Hector Mine earthquake, heavy black line denotes the simulated Hector Mine rupture, and green line denotes the true Hector Mine rupture. Other panels show time series of observed (grey stars) and modeled (solid blue line = biviscous model, solid red line = power law model) vertical displacement plotted for stations indicated with circles in Figures 9a and 9b.

A comparison to the assumed secular velocity (relative to station OPRD, as denoted by the dotted lines in Figure 8) shows that the coseismic stress changes remain essentially unrelaxed after 13 years of postseismic deformation. In contrast, the power law model indicates that horizontal velocities nearly returned to secular values by the end of the 13 year period. While neither model provides a satisfactory fit to all the data (possibly due to simplifications discussed above), it is worth noting that the biviscous model tends to overpredict the observed horizontal velocities, while the power law model generally underpredicts the data. Because the coseismic source is identical between the models, these differences are due to the assumed rheological properties alone. As one can see from Figure 9, a power law model provides a slightly better fit to the vertical GPS time series, both qualitatively and quantitatively, than does the biviscous

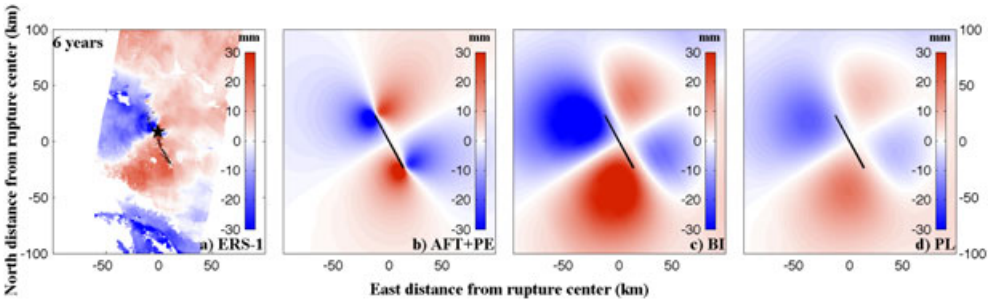

Figure 10. Six years of (a) observed and simulated ((b) afterslip + poroelastic; (c) biviscous; (d) power law) ERS-2 satellite line of sight displacement in millimeters. Black line in Figure 10a indicates true Hector Mine surface rupture and black star the Hector Mine epicenter; heavy black lines in Figures 10b–10d indicate simulated Hector Mine rupture.

model. The relative quality of fit is also illustrated in Figures S1b–S1d, which shows that the biviscous model has systematically higher misfits than the power law model for east, north, and vertical displacement components, regardless of which station is used as a reference site.

[29] InSAR observations provide an additional powerful constraint, as they are highly sensitive to vertical motion and have high spatial resolution. *Pollitz et al.* [2001] used several short-term (< 1 year) postseismic interferograms to argue that the polarity of the observed line of sight (LOS) displacements is consistent with a model postulating viscoelastic relaxation in the upper mantle. Unfortunately, InSAR imaging of postseismic deformation due to the Hector Mine earthquake was hampered by termination of the ERS-1 mission and failure of gyroscopes on the ERS-2 satellite. Nevertheless, one acquisition made by the ERS-2 satellite in December 2005 from the descending track 127 could be interfered with the immediate post earthquake acquisition of 20 October 1999. The respective interferogram is shown in Figure 10a. This interferogram does not appear to be affected by atmospheric noise; small atmospheric contributions on both acquisition dates (October 1999 and December 2005) are inferred based on analysis of multiple interferograms sharing the same acquisition date [e.g., *Fialko et al.*, 2002]. The data show pronounced lobes of LOS displacements to the west of the rupture and less deformation to the east of the rupture, similar to the pattern observed following the nearby 1992 Landers earthquake [*Fialko*, 2004a]. This qualitative similarity implies a common deformation mechanism. The amplitude of LOS displacements in anomalous lobes to the west of the Hector Mine rupture is of the order of ∼3 cm (Figure 10a).

[30] We compare the observed LOS displacements accumulated over a period of 6 years following the Hector Mine earthquake to predictions of our forward models assuming various candidate rheologies (Figure 10). For comparison, we also calculate LOS displacements for a model combining afterslip and poroelasticity, in the limit of full relaxation [*Barbot and Fialko*, 2010] (Figure 10b). The latter model assumes drained and undrained Poisson's ratio of 0.25 and 0.31, respectively. Parameters of the afterslip model were chosen a priori and were not adjusted to provide a better fit to the data. Surface displacements predicted by the three models are broadly similar, with quadrant patterns showing enhanced areas of range increase in the northwest and southeast quadrants of the rupture and range decrease in the southwest and northeast quadrants. LOS displacement amplitudes are enhanced on the west side of the rupture for all models, though the asymmetry is less pronounced for the combined afterslip/poroelastic model compared to the viscoelastic models. The size and shape of the LOS displacement quadrants vary. The biviscous model predicts fairly large quasi-circular lobes and high LOS displacement amplitudes compared to the observations (Figure 10c). The power law model predicts smaller lobes and lower amplitudes that slightly underpredict observed displacements (Figure 10d). The combined afterslip-poroelastic model appears to fit the observations west of the rupture reasonably well, consistent with findings of previous studies of postseismic deformation due to the Landers earthquake [*Peltzer et al.*, 1998; *Fialko*, 2004a]. However, this model overpredicts the amplitude of uplift in the northeast quadrant of the rupture. All three models show increases in the radar range in the southeast quadrant of the rupture, which are not seen in the data (Figure 10).

5. Discussion

5.1. The Effect of Shear Zones on Postseismic Deformation

[31] The postseismic velocity fields presented in Figures 3–6 allow for a straightforward comparison of models that do and do not incorporate thermally coupled shear zones. Early in the postseismic period, both the polarity and magnitude of vertical velocity are nearly indistinguishable for models WNS and WSZ. Horizontal velocities are also very similar for these two models within the first 10 years after the earthquake. Only later in the postseismic period, 50 years and more after the earthquake, do the velocity fields of these two models diverge, with a near-fault vertical polarity reversal and enhanced near-field fault-parallel velocities developing for model WSZ. However, after such a lengthy time period following the earthquake, horizontal and vertical postseismic transient velocities are small (∼1 mm/yr or less) and would thus be difficult to observe with modern geodetic techniques. The maximum magnitude of vertical velocity predicted for the reversed-polarity lobes in model WSZ never exceeds 0.3 mm/yr, and the respective deformation is thus essentially negligible.

[32] Models DNS and DSZ deviate to a greater extent than do models WNS and WSZ. The polarity of vertical velocity is reversed at all times for model DSZ relative

to DNS. Model DSZ also shows relatively high near-field fault-parallel velocity at all times. However, vertical velocities for these models never exceed 1 mm/yr. As such, the qualitative differences between models DNS and DSZ are likely unidentifiable from an observational standpoint, and these models fail to produce postseismic transients of sufficient amplitude.

[33] Model DSZ is the only viscoelastic model to predict the same vertical polarity pattern as the frictional afterslip model at all times in the postseismic period, illustrating that a thermally induced shear zone may qualitatively resemble the behavior of a frictional afterslip model. However, the magnitudes of postseismic velocity transients, particularly in the vertical direction, are negligible. Wet power law models do not qualitatively resemble the frictional afterslip model at any time during the postseismic period, save for a polarity reversal late in the postseismic period for model WSZ that would also be difficult to detect with geodetic measurements. It follows that even though thermally activated shear zones can in principle produce afterslip-like postseismic deformation, such strain localization can only occur if the background viscosity is very high, resulting in negligible postseismic transients. Weaker ductile materials are able to produce robust transients, but the strain localization in this case is insufficient to alter surface velocity patterns (in particular, the polarity of vertical velocities). This indicates that for the range of rheological properties considered in this study, shear heating and thermomechanical coupling are unable to generate surface velocity patterns similar to those due to afterslip.

[34] We note that smaller amplitudes of postseismic transients in case of stiffer rheologies may reflect a trade-off between the reduced effective viscosity and width of the shear zone. Specifically, changes in the rate of shear in response to a given stress change are directly proportional to the effective width of the shear zone, but inversely proportional to the effective viscosity of the shear zone. Because the degree of strain localization and the degree of weakening within the shear zone are related, the overall effect on transient deformation rates may be small. It follows that additional strain-weakening mechanisms may be needed to promote further strain localization and/or reduction in the effective viscosity within the shear zone.

[35] Potential candidates for additional weakening mechanisms are, e.g., dynamic recrystallization and foliation. Recrystallization and resulting grain-size reduction have been observed in ductile shear zones in nature [e.g., *Fitz Gerald and Stünitz*, 1993; *Jin et al.*, 1998] and laboratory experiments [e.g., *Tullis and Yund*, 1985; *Rutter*, 1995]. In our simulations of shear zone development, we have assumed that viscous deformation is governed by dislocation creep (equation (1)) and that thermal weakening serves as a proxy for all localization mechanisms. Explicit consideration of dynamic recrystallization requires that a diffusion creep term be added to the constitutive relation, such that

$$\dot{\varepsilon}_d = \dot{\varepsilon}_d^{(\mathrm{dis})} + \dot{\varepsilon}_d^{(\mathrm{diff})} = A_{\mathrm{dis}}\sigma_d^{n_{\mathrm{dis}}} \exp\left(-\frac{Q}{RT}\right) + A_{\mathrm{diff}} d^{-m} \sigma_d^{n_{\mathrm{diff}}}, \quad (11)$$

where $\dot{\varepsilon}_d^{(\mathrm{dis})}$ is the dislocation creep strain rate, $\dot{\varepsilon}_d^{(\mathrm{diff})}$ is the diffusion creep strain rate, A_{dis}, n_{dis}, and Q are the dislocation creep parameters (as in section 2.2), d is the grain size, m is the grain-size exponent, A_{diff} is the diffusion creep premultiplier, and $n_{\mathrm{diff}} = 1$ [*Poirier*, 1985]. In this formulation, diffusion creep is grain-size dependent, and dislocation creep is temperature dependent. Grain-size evolution and shear heating are stress-dependent processes [*Poirier*, 1985]; equation (3) and the dominant creep and localization mechanism in the combined creep law (equation (11)) depend largely on stress as well. The inclusion of grain-size-dependent diffusion creep in the flow law would thus likely alter the evolution of shear strain in the substrate. Our model does implicitly account for diffusion creep under the assumption that the contributions of $\dot{\varepsilon}_d^{(\mathrm{dis})}$ and $\dot{\varepsilon}_d^{(\mathrm{diff})}$ (equation (11)) are approximately equal [*De Bresser et al.*, 1998]. However, additional numerical experiments are needed to evaluate the effect of grain-size reduction on strain localization within ductile shear zones.

5.2. Implications for the Rheological Models of the Lithosphere in Eastern California

[36] As Figures 8 and 9 illustrate, proposed models of viscoelastic relaxation are able to fit the near-field horizontal and vertical velocities with variable degrees of success. We note that the comparison of model predictions to horizontal GPS displacements is somewhat difficult due to uncertainties in estimating the contribution of secular deformation. Fitting a linear trend to late post-Hector Mine time series is not sufficient to establish whether horizontal GPS velocities have returned to preseismic values 13 years following the event. Very few stations in the ECSZ were installed before the Hector Mine earthquake. In addition, the data may be affected by continuing postseismic deformation due to the 1992 Landers earthquake. Existing estimates of pre-Landers deformation rates based on trilateration and triangulation provide some constraint [*Savage et al.*, 2003] but suffer from large uncertainties. For example, studies of *Pollitz* [2003] and *Freed and Bürgmann* [2004] utilize secular loading rates that differ by a factor of two. Such a discrepancy can significantly affect the predicted time series and fits to the GPS observations. In particular, increasing the secular deformation rate by a factor of two compared to the value used in this study (10^{-7} year^{-1}) would cause the biviscous model to systematically overpredict the observed displacements and result in the power law model providing the better fit to data for nearly all stations. Vertical displacements might be less affected by uncertainties in secular deformation but are inherently noisier than the horizontal GPS displacements, which limits their discriminating power (e.g., see Figure 9, stations OPBL and WOMT). These results suggest that available GPS data are not sufficient for robust discrimination between the biviscous and power law rheologies proposed for the lower crust and upper mantle in Southeastern California.

[37] Additional constraints may be provided by InSAR data. For example, the biviscous model predicts continued uplift and subsidence beyond 10–20 years after the earthquake at rates that are ruled out by observations (Figure 10c). Calculations using the power law rheology proposed by *Freed and Bürgmann* [2004] underpredict LOS displacements immediately adjacent to the fault but are in better overall agreement with the InSAR data (Figure 10d). Near-field LOS displacements west of the fault may be better explained by the combined afterslip and poroelastic

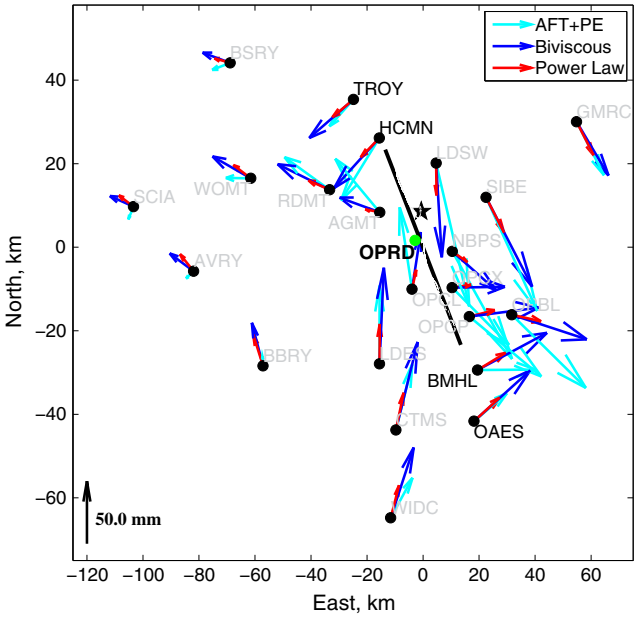

Figure 11. Predicted horizontal postseismic displacements for SCIGN GPS stations for full relaxation by combined afterslip and poroelastic effects (cyan arrows) and 13 years of relaxation by biviscous (blue arrows) and power law upper mantle flow (red arrows). Black star denotes the Hector Mine epicenter. Heavy black line indicates the simulated Hector Mine rupture.

model (Figure 10b). This model, however, underpredicts the asymmetry in the magnitudes of LOS displacements with respect to the fault plane (we reiterate that the parameters for the combined afterslip/poroelastic model were chosen a priori and not adjusted to provide a better fit to the data). The three tested models therefore provide comparable fits to the data, with no model reproducing the InSAR observations completely.

[38] We also investigated the amplitude of fault-perpendicular displacements along strike from the rupture that was proposed as a possible discriminant between viscoelastic relaxation and afterslip [e.g., *Hearn*, 2003]. In particular, viscoelastic relaxation is expected to produce significant fault-perpendicular displacements on the fault plane away from the earthquake rupture, while such displacements should be negligible in case of afterslip (Figures 3a–6a). However, poroelastic relaxation produces fault-perpendicular displacements on the nodal plane of a strike-slip fault that are comparable in magnitude and orientation to those due to viscoelastic relaxation (Figure 11). In addition, the rate at which nodal plane fault-perpendicular displacements decay with along-strike distance from the fault is similar for all three models (Figure 12). It follows that contributions from poroelastic rebound may obscure differences between afterslip and viscoelastic flow not only in case of vertical but also horizontal displacement patterns proposed as potential discriminants between the two mechanisms.

[39] The decade-long near-field observations of deformation following the Hector Mine earthquake further illustrate difficulties with using fault-perpendicular velocity components as a discriminant of the candidate mechanisms. As one can see from Figure 8, stations that are close to the main nodal plane at the north end of the earthquake rupture (TROY and HCMN) move in the fault-perpendicular direction during the postseismic period, consistent with both viscoelastic response and a combined afterslip-poroelastic relaxation (Figure 11). In contrast, stations to the south of the rupture (BMHL and OAES) exhibit postseismic displacements that are subparallel to the fault plane, with little or no fault-perpendicular velocity component. We note that local site effects at the reference station OPRD cannot be responsible for the different velocity patterns to the north and south of the Hector Mine rupture. To verify this, we added a constant translation to the entire array, such that the magnitudes of strike-parallel displacements at stations GMRC and BBRY, which are in approximately symmetric locations with respect to the fault plane (Figure S2), are nearly equal and in best agreement with the model predictions. Such a translation does not result in an antisymmetric pattern of fault-perpendicular displacements at the along-strike continuations of the rupture plane, as predicted by the three test models (Figure 11) and in fact degrades the quality of fit at both ends of the fault trace (Figure S2). These discrepancies may be due to essentially three-dimensional variations in material properties in the Earth crust (and, possibly, upper mantle). Such variations might also be responsible for the disagreement between the InSAR data and models in the southeastern quadrant of the rupture (Figure 10a).

[40] Far-field postseismic transients detected by GPS observations indicate that viscoelastic response in the mantle may indeed contribute to deformation following the Mojave desert earthquakes [*Freed et al.*, 2007]. The same observations have been subsequently used to suggest that a steady state mantle rheology inferred from laboratory experiments is not able to adequately explain the data and that transient creep laws may be required [*Freed et al.*, 2010], although time scales for transient creep inferred from laboratory experiments are of the order of 10^4–10^5 years

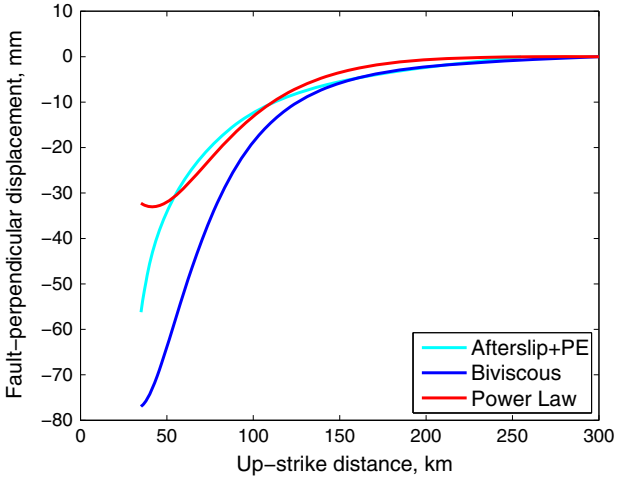

Figure 12. Predicted nodal plane fault-perpendicular postseismic displacements versus along-strike distance from the center of the fault plane, for full relaxation by combined afterslip and poroelastic (cyan line), and 13 years of relaxation by biviscous (blue line) and power law upper mantle flow (red line).

[e.g., *Smith and Carpenter*, 1987], much larger than the inferred duration of rapid postseismic deformation of the order of 10^{-1}–10^{0} years [e.g., *Pollitz*, 2003; *Freed et al.*, 2010]. We have not tested transient creep laws in the present study, but we note that the near-field data (where the signal-to-noise ratio is the highest) do not seem to require additional complexity. As a successful model (or family of models) must be able to explain both near-field and far-field observations, including both spatial and temporal patterns of surface velocity field, further work is warranted to understand the nature of postseismic deformation due to the Mojave Desert earthquakes, with emphasis on 3-D structure and material heterogeneities. Results presented in this study indicate that shear zones resulting from thermomechanical coupling do not significantly affect the predicted postseismic deformation due to the Landers and Hector Mine earthquakes (and, more generally, due to any large earthquake on a strike-slip fault) compared to predictions of viscoelastic models that assume a 1-D viscosity structure. Additional strain-weakening mechanisms are therefore necessary for the ductile fault roots to have an appreciable effect on transient surface deformation.

6. Conclusions

[41] We considered models of three-dimensional deformation resulting from a finite strike-slip rupture in an elastic crust underlain by a ductile substrate of various assumed rheologies. A subset of our models incorporated ductile shear zones generated by thermomechanical coupling and shear heating driven by long-term fault slip. Models including shear zones may be regarded as representing mature strike-slip faults, while models lacking shear zones may represent immature faults. We find that thermally induced shear zones do not appreciably alter surface deformation following a finite earthquake rupture. For a given loading rate, a rheologically weak (e.g., wet) substrate produces only moderate localization of strain. A strong (dry) substrate generates a high degree of localization but negligible deformation transients. Comparisons of model predictions to observations of postseismic deformation in the Eastern California Shear Zone suggest that available GPS and InSAR data do not allow one to distinguish viscoelastic relaxation models incorporating Burgers and power law rheologies on short (< 5 years) observation intervals. However, differences in the decay rate of the transient deformation predicted by the two models indicate that the models may be distinguished given continued GPS and InSAR monitoring on decadal timescales.

Appendix A: Burgers Rheology

[42] The shear relaxation modulus for a Burgers rheology with steady state and transient viscosities η_1 and η_2, respectively, and steady state and transient shear moduli μ_1 and μ_2, respectively, is [*Findlay et al.*, 1989]

$$G_R(t) = \frac{1}{A}[(q_1 - q_2 r_1)\exp(-r_1 t) - (q_1 - q_2 r_2)\exp(-r_2 t)], \quad \text{(A1)}$$

where

$$q_1 = 2\eta_1,\ q_2 = 2\frac{\eta_1\eta_2}{\mu_2},\ r_1 = \frac{p_1 - A}{2p_2},\ r_2 = \frac{p_1 + A}{2p_2}. \quad \text{(A2)}$$

with

$$p_1 = \frac{\eta_1}{\mu_1} + \frac{\eta_1}{\mu_2} + \frac{\eta_2}{\mu_2},\ p_2 = \frac{\eta_1\eta_2}{\mu_1\mu_2},\ A = \sqrt{p_1^2 - 4p_2}. \quad \text{(A3)}$$

The shear relaxation modulus may be represented by a dimensionless Prony series expansion

$$g_R(t) = \frac{G_R(t)}{G_0} = 1 - \sum_{i=1}^{N} \bar{g}_i^P \left(1 - \exp\left(\frac{-t}{\tau_i^G}\right)\right), \quad \text{(A4)}$$

by recognizing that if $C = (q_1 - q_2 r_1)/A$ and $D = (q_2 r_2 - q_1)/A$, equation (A1) may be expressed as

$$G_R(t) = (C + D) - [C(1 - \exp(-r_1 t)) + D(1 - \exp(-r_2 t))]. \quad \text{(A5)}$$

Normalizing by $G_0 = C + D$ yields the two-term dimensionless Prony series with $\bar{g}_1^P = C/(C + D)$, $\tau_1^G = 1/r_1$, $\bar{g}_2^P = D/(C + D)$, and $\tau_2^G = 1/r_2$.

Appendix B: Model Validation

[43] We benchmarked our finite element models against several available open-source semianalytical models. We used three codes to compare to predictions of the finite element model: RELAX [*Barbot and Fialko*, 2010], VISCO1D (F. Pollitz, http://earthquake.usgs.gov/research/software/), and PSGRN [*Wang et al.*, 2006]. RELAX and PSGRN use elastic Green's function approaches to calculate the mechanical response of a layered elastic/viscoelastic half space to fault slip; VISCO1D calculates postseismic deformation of a spherically stratified Earth model using a spherical harmonic expansion of global deformation modes and a sum of these modes for a given dislocation source. For simplicity, we replicate a published benchmark of strike-slip faulting in an elastic crust underlain by a Maxwell viscoelastic mantle [*Barbot and Fialko*, 2010]. Each model considered incorporates an identical 30 km thick elastic crust, with a shear modulus of 30 GPa and Poisson's ratio of 0.25. The Abaqus finite element model assumes a 270 km thick upper mantle. The RELAX and PSGRN models assume half space mantles. VISCO1D model assumes a 6431 km radius spherical mantle (total earth radius of 6371 km). The mantle in all models is composed of a Maxwell viscoelastic material with a relaxation time τ_r of 10 years.

[44] Figure S3 shows the surface displacement predicted by each of the four models at $t = 2\tau_r = 20$ years after the coseismic rupture. A generally good agreement (relative errors less than 18%) is achieved among the four models in both the horizontal and vertical components of displacement.

[45] In order to test our implementation of the Burgers body rheology, we also compare the results of an Abaqus model with those from a VISCO1D model, which is the only semianalytical code of the three tested that is able to implement a Burgers rheology. The models tested assume the rheological layering and properties of model BI, discussed in section 2.2. However, in the benchmark models, the fault penetrates to 10 km depth, rooting in the elastic upper crust. The shallower fault tip is necessary because VISCO1D is not capable of treating fault slip in a viscoelastic material. Figure S4 shows surface velocities plotted at $t = 6$ months and $t = \tau_1 = 2$ years, the latter being the steady state

relaxation time of the Burgers material. While some differences may be observed between the two models, namely in the far-field vertical velocities, the Abaqus model captures maximum amplitudes of the vertical and horizontal velocities within 15%.

[46] **Acknowledgments.** This work was funded by the National Science Foundation (grant EAR-1321932) and the Southern California Earthquake Center. We thank Paul Segall, an anonymous reviewer, and an associate editor for their insightful comments. We also thank Sylvain Barbot and Fred Pollitz for their assistance with RELAX and VISCO1D, respectively. Finite element meshes were created using code APMODEL, courtesy of S. Kenner.

References

Barbot, S., and Y. Fialko (2010), A unified continuum representation of post-seismic relaxation mechanisms: Semi-analytic models of afterslip, poroelastic rebound and viscoelastic flow, *Geophys. J. Int.*, *182*, 1124–1140.

Barbot, S., Y. Fialko, and Y. Bock (2009), Postseismic deformation due to the Mw 6.0 2004 Parkfield earthquake: Stress-driven creep on a fault with spatially variable rate-and-state friction parameters, *J. Geophys. Res.*, *114*, B07405, doi:10.1029/2008JB005748.

Booker, J. (1974), Time dependent strain following faulting of a porous medium, *J. Geophys. Res.*, *79*(14), 2037–2044, doi:10.1029/JB079i014p02037.

De Bresser, J., C. Peach, J. Reijs, and C. Speirs (1998), On dynamic recrystallization during solid state flow: Effects of stress and temperature, *Geophys. Res. Lett.*, *25*, 3457–3460.

Dieterich, J. (1978), Time-dependent friction and the mechanics of stick-slip, *Pure Appl. Geophys.*, *116*, 790–806, doi:10.1007/BF00876539.

Dokka, R., and C. Travis (1990), Role of the Eastern California Shear Zone in accommodating Pacific-North American plate motion, *Geophys. Res. Lett.*, *17*, 1323–1326.

Dreger, D., and A. Kaverina (2000), Seismic remote sensing for the earthquake source process and near-source strong shaking: A case study of the October 16, 1999 Hector Mine earthquake, *Geophys. Res. Lett.*, *27*, 1941–1944.

Elsasser, W. (1969), Convection stress propagation in the upper mantle, in *The Application of Modern Physics to the Earth and Planetary Interiors*, edited by S. K. Runcom, pp. 223–246, Wiley-Interscience, London, U.K.

Fialko, Y. (2004a), Evidence of fluid-filled upper crust from observations of postseismic deformation due to the 1992 M_w7.3 Landers earthquake, *J. Geophys. Res.*, *109*, B08401, doi:10.1029/2004JB002985.

Fialko, Y. (2004b), Probing the mechanical properties of seismically active crust with space geodesy: Study of the co-seismic deformation due to the 1992 M_w7:3 Landers (Southern California) earthquake, *J. Geophys. Res.*, *109*, B03307, doi:10.1029/2003JB002756.

Fialko, Y., D. Sandwell, D. Agnew, M. Simons, P. Shearer, and B. Minster (2002), Deformation on nearby faults induced by the 1999 Hector Mine Earthquake, *Science*, *297*, 1858–1862, doi:10.1126/science.1074671.

Findlay, W., J. Lai, and K. Onaran (1989), *Creep and Relaxation of Nonlinear Viscoelastic Materials*, 371 p., Dover Publishing, New York.

Fitz Gerald, J., and H. Stünitz (1993), Deformation of granitoids at low metamorphic grade. I: Reactions and grain size reduction, *Tectonophysics*, *221*, 269–297.

Freed, A., and R. Bürgmann (2004), Evidence of power-law flow in the Mojave desert mantle, *Nature*, *430*, 548–551, doi:10.1038/nature02784.

Freed, A., R. Bürgmann, and T. Herring (2007), Far-reaching transient motions after Mojave earthquakes require broad mantle flow beneath a strong crust, *Geophys. Res. Lett.*, *34*, L19302, doi:10.1029/2007GL030959.

Freed, A., T. Herring, and R. Bürgmann (2010), Steady-state laboratory flow laws alone fail to explain postseismic observations, *Earth Planet. Sci. Lett.*, *300*, 1–10, doi:10.1016/j.epsl.2010.10.005.

Hearn, E. (2003), What can GPS data tell us about the dynamics of post-seismic deformation?, *Geophys. J. Int.*, *155*, 753–777, doi:10.1029/JB095iB04p04873.

Hearn, E., S. McCluskey, S. Ergintav, and R. Reilinger (2009), Izmit earthquake postseismic deformation and dynamics of the North Anatolian Fault Zone, *J. Geophys. Res.*, *114*, B08405, doi:10.1029/2008JB006026.

Hetland, E. A., and B. H. Hager (2006), Interseismic strain accumulation: Spin-up, cycle invariance, and irregular rupture sequences, *Geochem. Geophys. Geosyst.*, *7*, Q05004, doi:10.1029/2005GC001087.

Hirth, G., and D. Kohlstedt (2004), Rheology of the upper mantle and mantle wedge: A view from the experimentalists, in *Inside the Subduction Factory, Geophys. Monogr. Ser.,* vol. 138, edited by J. Eiler, pp. 83–105, AGU, Washington, D. C.

Jacobs, A., D. Sandwell, Y. Fialko, and L. Sichoix (2002), The 1999 (Mw7.1) Hector Mine, California, earthquake: Near-field postseismic deformation from ERS interferometry, *Bull. Seism. Soc. Am.*, *92*, 1433–1442.

Jin, D., S.-I. Karato, and M. Obata (1998), Mechanisms of shear localization in the continental lithosphere: Inference from the deformation microstructures from the Ivrea zone, Northwest Italy, *J. Struct. Geol.*, *20*, 195–209.

Jonsson, S., P. Segall, R. Pedersen, and G. Bjornsson (2003), Post-earthquake ground movements correlated to pore-pressure transients, *Nature*, *424*, 179–183.

Kanamori, H., H. Thio, D. Dreger, E. Hauksson, and T. Heaton (1992), Initial investigation of the Landers, California, earthquake of 28 June 1992 using TERRAscope, *Geophys. Res. Lett.*, *19*, 2267–2270.

Karato, S., and P. Wu (1993), Rheology of the upper mantle: A synthesis, *Science*, *260*, 771–778, doi:10.1126/science.260.5109.771.

Kenner, S., and P. Segall (2003), Lower crustal structure in northern California: Implications from strain rate variations following the 1906 San Francisco earthquake, *J. Geophys. Res.*, *108*(B1), 2011, doi:10.1029/2001JB000189.

Kirby, S., and A. Kronenburg (1987), Rheology of the lithosphere: Selected topics, *Rev. Geophys.*, *25*, 1219–1244.

Mackwell, S., M. Zimmerman, and D. Kohlstedt (1998), High-temperature deformation of dry diabase with application to tectonics on Venus, *J. Geophys. Res.*, *103*, 975–984, doi:10.1029/97JB02671.

Massonnet, D., W. Thatcher, and H. Vadon (1996), Detection of postseismic fault-zone collapse following the Landers earthquake, *Nature*, *382*, 612–616.

Masterlark, T., and H. Wang (2002), Transient stress-coupling between the 1992 Landers and 1999 Hector Mine, California, earthquakes, *Bull. Seism. Soc. Am.*, *92*, 1470–1486.

Nur, A., and G. Mavko (1974), Postseismic viscoelastic rebound, *Science*, *183*, 204–206, doi:10.1126/science.183.4121.204.

Peltzer, G., P. Rosen, F. Rogez, and K. Hudnut (1998), Poroelastic rebound along the Landers 1992 earthquake surface rupture, *J. Geophys. Res.*, *103*(B12), 30,131–30,145.

Poirier, J. (1985), *Creep of Crystals: High-Temperature Deformation Processes in Metals, Ceramics and Minerals*, 276 pp., Cambridge Univ. Press, Cambridge, U.K.

Pollitz, F. (1997), Gravitational viscoelastic postseismic relaxation on a layered spherical Earth, *J. Geophys. Res.*, *102*, 17,921–17,941.

Pollitz, F. (2003), Transient rheology of the uppermost mantle beneath the Mojave Desert, California, *Earth Planet. Sci. Lett.*, *215*, 89–104, doi:10.1016/S0012-821X(03)00432-1.

Pollitz, F., G. Peltzer, and R. Bürgmann (2000), Mobility of continental mantle: Evidence from postseismic geodetic observations following the 1992 Landers earthquake, *J. Geophys. Res.*, *105*, 8035–8054, doi:10.1029/1999JB900380.

Pollitz, F., Wicks. C., and W. Thatcher (2001), Mantle flow beneath a continental strike-slip fault: Postseismic deformation after the 1999 Hector Mine earthquake, *Science*, *293*, 1814–1818.

Rudnick, R., and D. Fountain (1995), Nature and composition of the continental crust: A lower crustal perspective, *Rev. Geophys.*, *33*, 267–309, doi:10.1029/95RG01302.

Ruina, A. (1983), Slip instability and state variable friction laws, *J. Geophys. Res.*, *88*, 10,359–10,370.

Rutter, E. (1995), Experimental study of the influence of stress, temperature, and strain on the dynamic recrystallization of Carrara marble, *J. Geophys. Res.*, *100*, 24,651–24,663, doi:10.1029/95JB02500.

Savage, J. (1990), Equivalent strike-slip earthquake cycles in half-space and lithosphere-asthenosphere Earth models, *J. Geophys. Res.*, *95*, 4873–4879, doi:10.1029/JB095iB04p04873.

Savage, J., and W. Prescott (1978), Asthenosphere readjustment and the earthquake cycle, *J. Geophys. Res.*, *83*, 3369–3376.

Savage, J., J. Svarc, and W. Prescott (2003), Near-field postseismic deformation associated with the 1992 Landers and 1999 Hector Mine, California, earthquakes, *J. Geophys. Res.*, *108*(B9), 2432, doi:10.1029/2002JB002330.

Shelton, G., and J. Tullis (1981), Experimental flow laws for crustal rocks, *Eos Trans. AGU*, *62*, 396.

Sieh, K., et al. (1993), Near-field investigations of the Landers earthquake sequence, April to July 1992, *Science*, *260*, 171–176.

Simons, M., Y. Fialko, and Y. Rivera (2002), Coseismic deformation from the 1999 Mw 7.1 Hector Mine, California, earthquake as inferred from InSAR and GPS observations, *Bull. Seismol. Soc. Am.*, *92*, 1390–1402, doi:10.1111/j.1365-246X.2010.04678.x.

Smith, B., and F. Carpenter (1987), Transient creep in orthosilicates, *Phys. Earth Planet. Inter.*, *49*, 314–324, doi:10.1016/0031-9201(87)90033-1.

Takeuchi, C., and Y. Fialko (2012), Dynamic models of interseismic deformation and stress transfer from plate motion to continental transform faults, *J. Geophys. Res.*, *117*, B05403, doi:10.1029/2011JB009056.

Tse, S., and J. Rice (1986), Crustal earthquake instability in relation to the depth variation of frictional slip properties, *J. Geophys. Res.*, *91*(B9), 9452–9472.

Tullis, J., and R. Yund (1985), Dynamic recrystallization of feldspar: A mechanism for ductile shear zone formation, *Geology*, *91*, 238–241.

Wang, R., F. Lorenzo-Martin, and F. Roth (2006), PSGRN/PSCMP—A new code for calculating co- and post-seismic deformation, geoid and gravity changes based on the viscoelastic-gravitational dislocation theory, *Comput. Geosci.*, *32*, 527–541.